Manganese-Iron Phosphate Nodules at the Groken Site, Gale Crater, Mars

Allan H. Treiman [1,*], Nina L. Lanza [2], Scott VanBommel [3], Jeff Berger [4], Roger Wiens [5], Thomas Bristow [6], Jeffrey Johnson [7], Melissa Rice [8], Reginald Hart [8], Amy McAdam [9], Patrick Gasda [2], Pierre-Yves Meslin [10], Albert Yen [11], Amy J. Williams [12], Ashwin Vasavada [11], David Vaniman [13], Valerie Tu [14], Michael Thorpe [9], Elizabeth D. Swanner [15], Christina Seeger [16], Susanne P. Schwenzer [17], Susanne Schröder [18], Elizabeth Rampe [14], William Rapin [19], Silas J. Ralston [4], Tanya Peretyazhko [4], Horton Newsom [20], Richard V. Morris [14], Douglas Ming [14], Matteo Loche [10], Stéphane Le Mouélic [21], Christopher House [22], Robert Hazen [23], John P. Grotzinger [16], Ralf Gellert [24], Olivier Gasnault [8], Woodward W. Fischer [16], Ari Essunfeld [2], Robert T. Downs [25], Gordon W. Downs [25], Erwin Dehouck [26], Laura J. Crossey [20], Agnes Cousin [10], Jade M. Comellas [27], Joanna V. Clark [16], Benton Clark III [28], Steve Chipera [13], Gwenaël Caravaca [29], John Bridges [30], David F. Blake [6] and Ryan Anderson [31]

[1] Lunar and Planetary Institute, Universities Space Research Association, 3600 Bay Area Blvd., Houston, TX 77058, USA
[2] Los Alamos National Laboratory, Los Alamos, NM 87545, USA; nlanza@lanl.gov (N.L.L.); gasda@lanl.gov (P.G.)
[3] McDonnell Center for the Space Sciences, Department of Earth and Planetary Sciences, Washington University in St. Louis, St. Louis, MO 63130, USA
[4] Jacobs—JETS, NASA Johnson Space Center, Houston, TX 77058, USA; jeff.berger@nasa.gov (J.B.); silas.ralston@nasa.gov (S.J.R.); tanya.peretyazhko@nasa.gov (T.P.)
[5] Earth, Atmospheric, and Planetary Sciences, Purdue University, West Lafayette, IN 47907, USA; rwiens@purdue.edu
[6] NASA Ames Research Center, Mountain View, CA 94035, USA; thomas.f.bristow@nasa.gov (T.B.)
[7] Johns Hopkins University Applied Physics Laboratory, Laurel, MD 20723, USA
[8] Geology Department, Western Washington University, Bellingham, WA 98225, USA; ricem5@wwu.edu (M.R.); olivier.gasnault@irap.omp.eu (O.G.)
[9] NASA Goddard Space Flight Center, Greenbelt, MD 20771, USA; michael.t.thorpe@nasa.gov (M.T.)
[10] Institut de Recherche en Astrophysique et Planétologie, Université de Toulouse, CNRS, UPS, CNES, Observatoire Midi-Pyrénées, 31400 Toulouse, France; pmeslin@irap.omp.eu (P.-Y.M.)
[11] Jet Propulsion Laboratory, California Institute of Technology, Pasadena, CA 91109, USA; albert.s.yen@jpl.nasa.gov (A.Y.); ashwin.r.vasavada@jpl.nasa.gov (A.V.)
[12] Department of Geological Sciences, University of Florida, Gainsville, FL 32611, USA; amywilliams1@ufl.edu
[13] Planetary Science Institute, Tucson, AZ 85719, USA; dvaniman@psi.edu (D.V.)
[14] NASA Johnson Space Center, Houston, TX 77058, USA; elizabeth.b.rampe@nasa.gov (E.R.); richard.v.morris@nasa.gov (R.V.M.)
[15] Geological and Atmospheric Sciences, Iowa State University, Ames, IA 50011, USA; eswanner@iastate.edu
[16] California Institute of Technology, Pasadena, CA 91125, USA; cseeger@caltech.edu (C.S.); wfischer@caltech.edu (W.W.F.)
[17] OUAstrobiology, Open University, Milton Keynes MK7 6AA, UK; susanne.schwenzer@open.ac.uk
[18] Deutsche Zentrum für Luft- und Raumfahrt (DLR), Institute of Optical Sensor Systems, 12489 Berlin, Germany; susanne.schroeder@dlr.de
[19] Institut de Recherche en Astrophysique et Planétologie, Toulouse, France; william.rapin@irap.omp.eu
[20] Earth and Planetary Sciences, University of New Mexico, Albuquerque, NM 87106, USA; newsom@unm.edu (H.N.); lcrossey@unm.edu (L.J.C.)

[21] Laboratoire de Planétologie et Géosciences, UMR CNRS 6112, Nantes Université, Université d'Angers, 49000 Angers, France
[22] College of Earth and Mineral Sciences, The Pennsylvania State University, State College, PA 16802, USA
[23] Geophysical Laboratory, Carnegie Institution, Washington, DC 20015, USA
[24] Physics Department, University of Guelph, Guelph, ON N1G 2W1, Canada
[25] Department of Geosciences, University of Arizona, Tucson, AZ 85721, USA; rdowns@arizona.edu (R.T.D.)
[26] Laboratoire de Géologie de Lyon: Terre, Planètes, Environnement, Université Lyon, 69622 Villeurbanne, France
[27] Hawai'i Institute of Geophysics and Planetology, University of Hawai'i at Mānoa, Honolulu, HI 96822, USA
[28] Space Sciences Institute, Boulder, CO 80301, USA
[29] Institut de Recherche en Astrophysique et Planetologie, Universite Paul Sabatier Toulouse III, Toulouse, France
[30] Department of Physics and Astronomy, University of Leicester, Leicester LE1 7RH, UK
[31] US Geological Survey, Astrogeology Center, Flagstaff, AZ 86001, USA
* Correspondence: treiman@lpi.usra.edu

TIMELINES OF CURIOSITY AT MOZIE_LAW AND GROKEN

	Rover Operations Timeline
Sol	Action
2810	map out path to Mozie_Law
2829	arrive at Mozie_Law site; recognition of Groken/Ayton nodules
2838	Drill Mary_Anning - ccam 4x4 Ayton nodules
2870	Drill Mary_Anning3
2904	Bump to Ayton / Groken
2910	Drill Groken
2923	Leave Mozie_Law

	SAM Timeline
Sol	Action
2778	Mahaffy science discussion for TMAH find suitable location
2810	SAM request to return to a Glen_Etive equivalent for TMAH analysis
	Mozie_Law area selected as stratigraphically equivalent
2844	SAM EGA analysis of Mary_Anning sample
2849	SAM second dropoff of Mary_Anning for EGC & GCMS
2879	SAM TMAH Mary_Anning3
2895	SAM wet chem of Mary_Anning3
2918	SAM EGA of Groken

	APXS Timeline
Sol	Analysis
2826	Breamish_Offset: DRT MnO~0.8%
2833	MaryAnning_DRT: offset MnO~0.5%
2851	MaryAnning_Dump1 & 2
2853	MaryAnning_tailings
2857	Ayton_raster1-3, for deconvolution analysis
2858	MaryAnning2_DRT & offset
2862	Falkirk_Wheel & offset ~1% MnO
2867	MaryAnning3_DRT & offset
2890	MaryAnning3_Dump1 & 2
2906	Groken offset & Groken DRT
2908	Trow offset & Trow drt
2920	Groken dump1 & dump2 (no Groken material)
2921	Groken drill cuttings

	CheMin Timeline
Sol	Action
2912	CheMin Groken dropoff to Chmn & first analysis. pristine Mylar cell 9A
2913	CheMin Downlink data from first analysis

2914	CheMin Second analysis of Groken (PUL1 Craig; PUL2 Treiman)G
2915	CheMin Downlink data from second analysis
2922	CheMin Third analysis of Groken (plan on 2921)
2925	CheMin Downlink data from third Groken analysis
2930	CheMin Fourth analysis of Groken - kumbayatic vibe
2932	CheMin Downlink data from fourth Groken analysis
2934	CheMin Dump Groken sample
2944	CheMin Uplink raw frames return first batch (plan 2942). CheMin minor frames 1-4: 720 total raw frames
2963	CheMin Raw frames start coming down
2966	CheMin Raw frames still coming down
2970	CheMin Raw Frames received
2969	CheMin Uplink second and third raw frame returns. (minor frames 5-12: 1440 raw frames)
2979	CheMin Uplink fourth raw frame returns. minor frames 13-15: 540 raw frames)
2983	CheMin raw frames still being downlinked
3001	CheMin Uplink analysis and get-data of empty cell 9A

ChemCam timeline; LIBS analyses unless otherwise noted.

2834	Mary_Anning_ccam1, High Mn pt 5
2834	Mary_Anning_ccam2, moderate Mn.
2837	Mary_Annin_DrillTailings_ccam, FAILed
2837	Mary_Anning_Zstack_ccam,
2837	Ayton, high Mn points associated with dark nodules. The highest points in Mn (1, 2, 4, 11) are associated with the dark nodules in the bedrock and elevated MgO and FeO contents, with a detectable P signal and lower total elements.
2841	Mary_Anning_ccam_2839, 2x5 drill hole wall
2841	Geike, 10x1 bedrock, no nodules Mn slightly elevated
2841	Fearns, 10x1 becrock, high MnO
2841	Mary_Anning_tailings_2838, 5x1 passive
2841	Great Trossachs, float rock 5x1 high Mn
2842	Bishops_Palace, 10x1 bedrock “Mn detection”
2843	Mary_Anning_drill_hole, Zstack RMI
2847	Musselburgh, high Mn and P detection on pt 7
2848	Mary_Anning_ccam_2846, pt 6 has elevated Mn, H, and P)
2849	Ayton_2, Mn high in pts 2, 5; high H detected P in pit 5
2852	Mary_Anning_ccam_2851, LIBS in drill hole.
2852	Mary_Anning_dump_ccam, dump pile likely blew away
2852	Ayton_2_dp, depth profile, little change with depth
2862	Tray, homogeneous target, no high Mn
2862	Tain, bedrock, pt 4 has high Mn and detected P
2863	Falkirk_Wheel, pt 10 on dark nodule, high Mn, H, detected P
2864	Howwood, most points rich in Mn, peaks for H and P
2865	Maligar, first five points rich in Mn, peaks for H and P
2865	North_Fearns, point 4 rich in Mn, peaks for H and P
2867	Formartine, Pt 10 elevated Mn, P.

2868	Foulden, pt 6 elevated Mn, P, Mg, H.
2869	Mary_Anning_3_ccam, pre-drill
2871	Mary_Anning_3_drill_tailings, ccam2
2872	Mary_Anning3, RLR down drill hole, RMI
2872	Ayton_APXS_ccam
2876	Njuggleswater, pts7,10 rich in Mn, H, detected P
2872	Toab, all 10 have high Mn, esp 1,3,4,7
2876	Mary_Anning_3_drill_tailings, passive raster
2882	Le-Ceasnachadh, passive, RMI
2883	Le-Ceasnachadh_2 passive, RMI
2883	Sandlodge_Mine, pt 5 very high Mn.
2886	Le-Ceasnachadh_3 passive
2886	Lealt, pts 7 & 8 have high Mn
2891	Mary_Anning_3_dump_pile
2891	Lunnasting, pt 2 has high Mn H detected P
2891	Kleber, several high Mn incl #5 with P and H
2902	Wart, All points are high in Mn, #7 is in particular elevated and hit dark material, has highest MgO and FeOT, lowest totals, strong H and P detections.
2902	Balallan, Mn is high in all points and #10 is particular Mn-rich, also with high MgO, & strongest H of this target but no obvious P detection.
2906	Groken_ccam
2906	Hella, high Mn in points 1, 4, 6.
2907	Great_Skua, high Mn & detectable H across all
2912	Groken_ccam2
2913	Groken_Drill_Tailings_ccam1, & -ccam2

MASTCAM MULTISPECTRAL

By Melissa Rice and Reginald Hart.

Mastcam multispectral observations, visible to near-infrared, were acquired for several fields of view in the Mozie_Law area. Of particular interest here are those of the Groken drill site area with its nodules and of the Le_Caesnachadh rock. Processing and interpretation of these spectra follow the procedures of [4].

Mastcam spectra of the Groken drill site were extracted from an observation acquired after drilling (Figure S1). Comparison to reflectance spectra of the nodules from before drilling show no change in nodule properties; the pixels chosen for both sets of compiled spectra were somewhat distant from the drill hole site and (fortuitously) upwind from the Groken drill hole. Both rock and nodule spectra show increasing reflectance from 400 through ~800 nm wavelengths, and a broad absorption centered at ~850-900 nm (Figure S1). These features are consistent with the presence of hematite in grains on the order of 45 μm diameter. The nodule spectra are considerably darker (lower reflectance) in the red- to near-infrared wavelengths than the non-nodular rock spectra (Figure S1). The "uptick" in reflectance at ~440 nm for the Groken nodules spectrum is a known artifact [4]. This difference suggests that the nodules contain a substance with low reflectance and no strong absorption features, i.e., spectrally bland, in the visible-to-near-infrared wavelengths. Among such substances are pyrolusite (MnO_2) and magnetite (Fe_2O_3)

The Le_Caesnachadh rock lay several meters from the Mozie_Law slab (main text, Figure 1B), and is one of the few local rocks besides Mozie_Law that contains abundant dark angular nodules. ChemCam passive spectra were acquired for Le_Caesnachadh, making it the only nodular rock for which we have both Mastcam multispectral and ChemCam passive reflectance spectra (main text, Figure 8). Mastcam multispectral data for Le_Caesnachadh are shown in Figure S2; the reflectance spectra of the nodules and of the non-nodular rock are effectively identical to those of similar material at the Groken site (Figure S1). It seems likely, then, that the Le_Caesnachadh nodules are essentially the same as those at Groken, and that the ChemCam passive spectrum of the Le_Caesnachadh nodules is relevant to those at Groken.

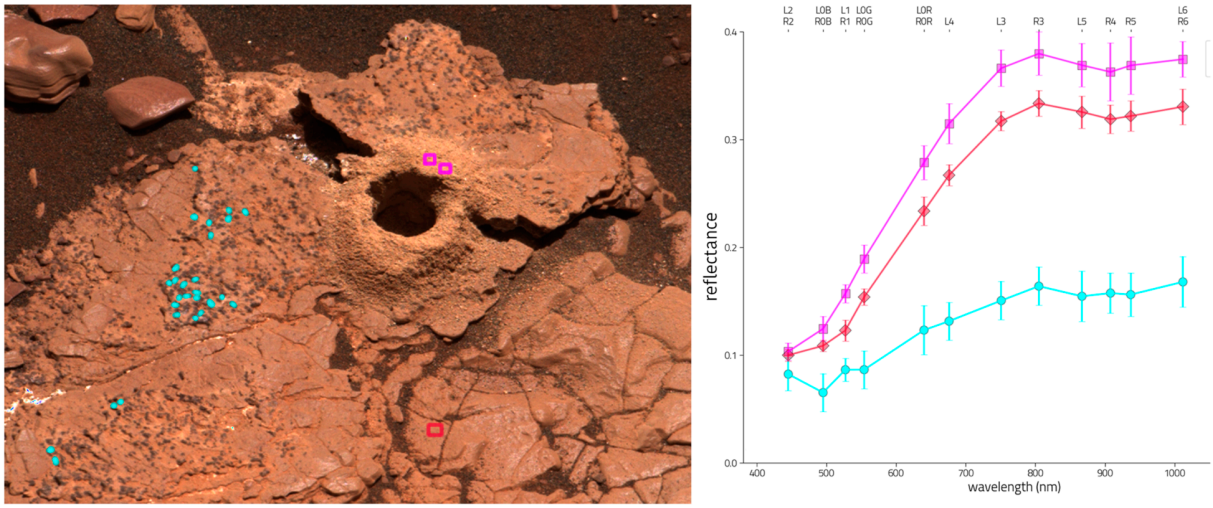

Figure S1. Mastcam multispectral reflectance observation in the Groken area, post-drilling, sol 2911, sequence identifier mcam15193. See also Figures 2A,C of main text. Left: Mastcam R0 image annotated with regions of interest (ROIs) from which pixels were averaged to extract reflectance spectra of drill tailings (magenta), outcrop (red) and nodules (cyan). Right: relative reflectance spectra averages for the ROIs shown at left. All spectra indicate a broad absorption centered around 900 nm, which is consistent with fine-grained hematite and other Fe-oxides. The spectrum of the drill cuttings is the same as that of the rock, only brighter (which we attribute to its finer grainsize). The nodule material is much darker, suggesting that there can be little nodule material in the drill cuttings. The low reflectances of the nodules suggests the presence of a dark, spectrally bland material, possibly pyrolusite or magnetite.

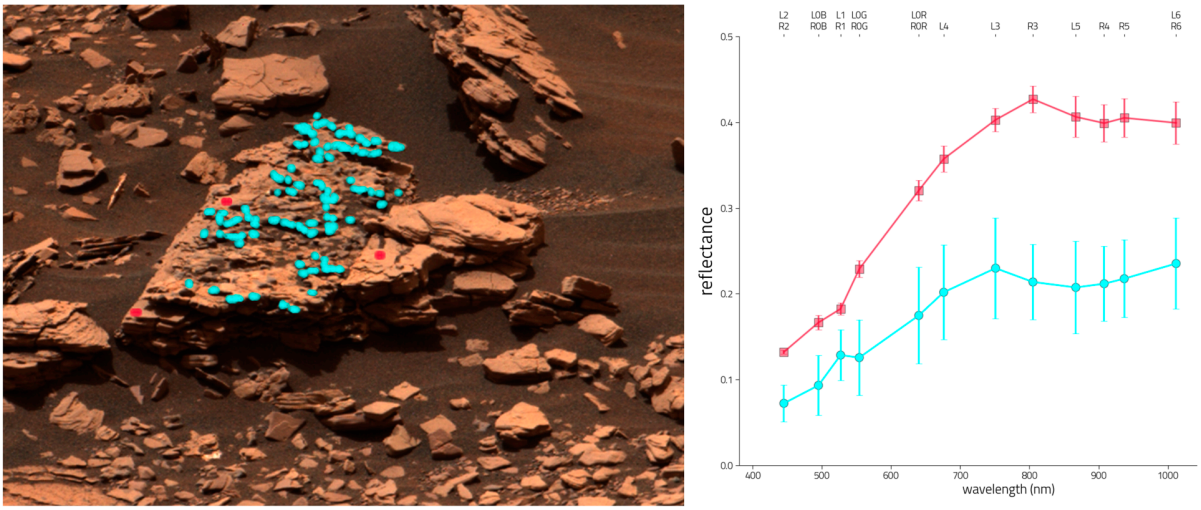

Figure S2. Mastcam multispectral observation of the Le_Caesnachadh rock, the only nodular rock in the area for which ChemCam passive spectra were acquired, sol 2882, sequence identifier mcam15033. See also Figure 2F of main text. Left: Mastcam R0 image annotated with regions of interest (ROIs) from which pixels were averaged to extract reflectance spectra of outcrop (red) and nodules (cyan). Right: relative reflectance spectra averages for the ROIs shown at left. Both rock and nodules spectra have broad absorptions centered around 900 nm, which are consistent with fine-grained hematite and other Fe-oxides. The nodule spectrum is darker, suggesting presence of a dark, spectrally bland material, possibly pyrolusite or magnetite. The nodule spectrum is consistent with that acquired by ChemCam passive of the same area (Figure 8A of main text), given the variation in illumination conditions.

ADDITIONAL LIBS DATA

A crucial question from the main text is the abundances of SiO_2 in the Groken nodules. The APXS Ayton deconvolution [2] shows no SiO_2 (Table 3 of main text), while the LIBS analyses show SiO_2 around 44% wt (Table 4 and Figure 7B of main text). To support the LIBS analyses, Figure S3 shows LIBS emission spectra (summed over all LIBS laser shots) for the Ayton_APXS_ccam raster, same as shown in Table 4 and Figure 7 of the main text. All the spectra show a distinct emission of Si at 288 nm, at approximately the same intensity, suggesting essentially consistent abundances of SiO_2 independent of whether the spectra represent a target on or off of a dark Mn-P rich nodule, see Figure S4 (and Figure 7A,B in main text).

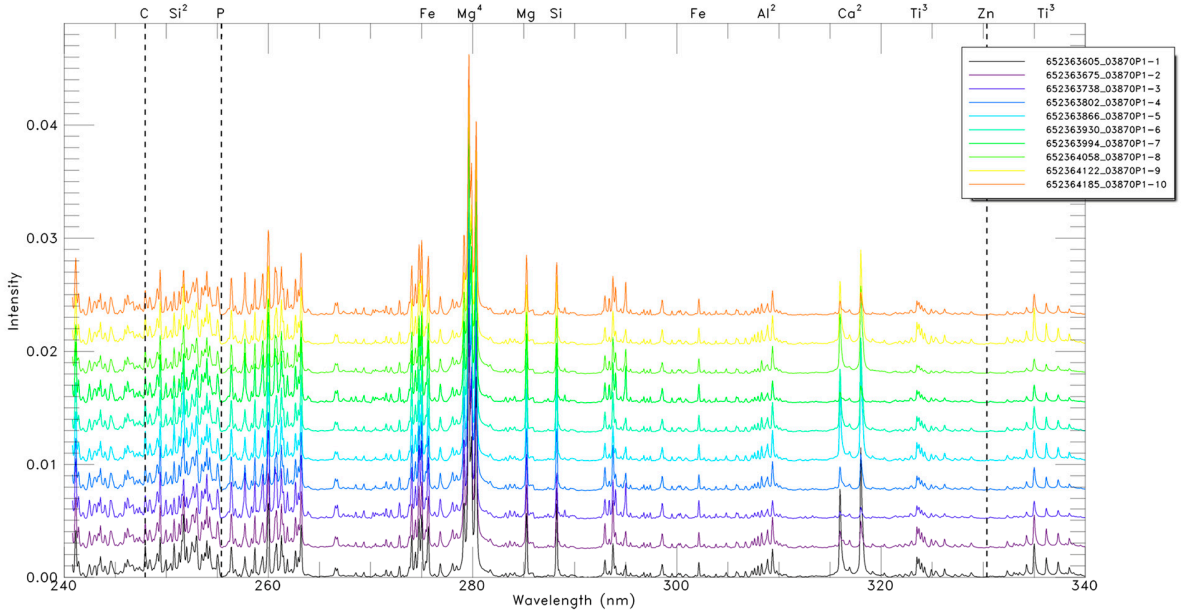

Figure S3. ChemCam LIBS emission spectra, emphasizing Si and Al photoemissions, for targets in the raster Ayton_APXS_ccam (sol 2872). Each colored line is a target spectrum (numbering as in Figure 6A of main text), offset vertically for clarity. The Si 288 nm peak and Al 309 nm peaks are apparent in every spectrum from the raster, notably for dark, Mn-rich targets 3, 7, 8 and 10, (see Figure S4).

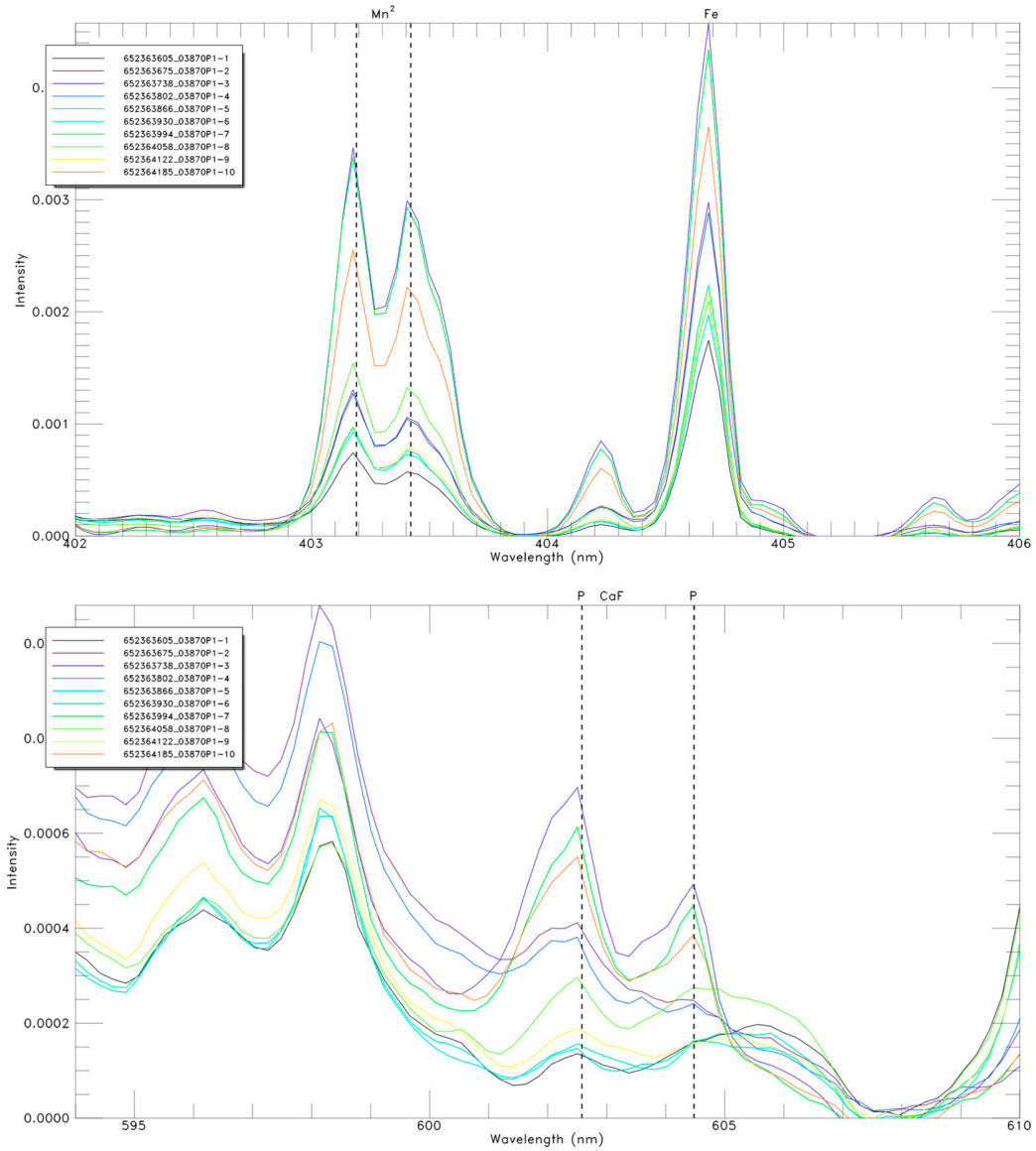

Figure S4. ChemCam LIBS emission spectra for targets in the raster Ayton_APXS_ccam (sol 2872). See Figure 7 of main text. Each colored line is a target spectrum, not offset vertically. A) Spectrum range including strongest emission lines for Mn. B) Spectrum range including strongest emission lines for P.

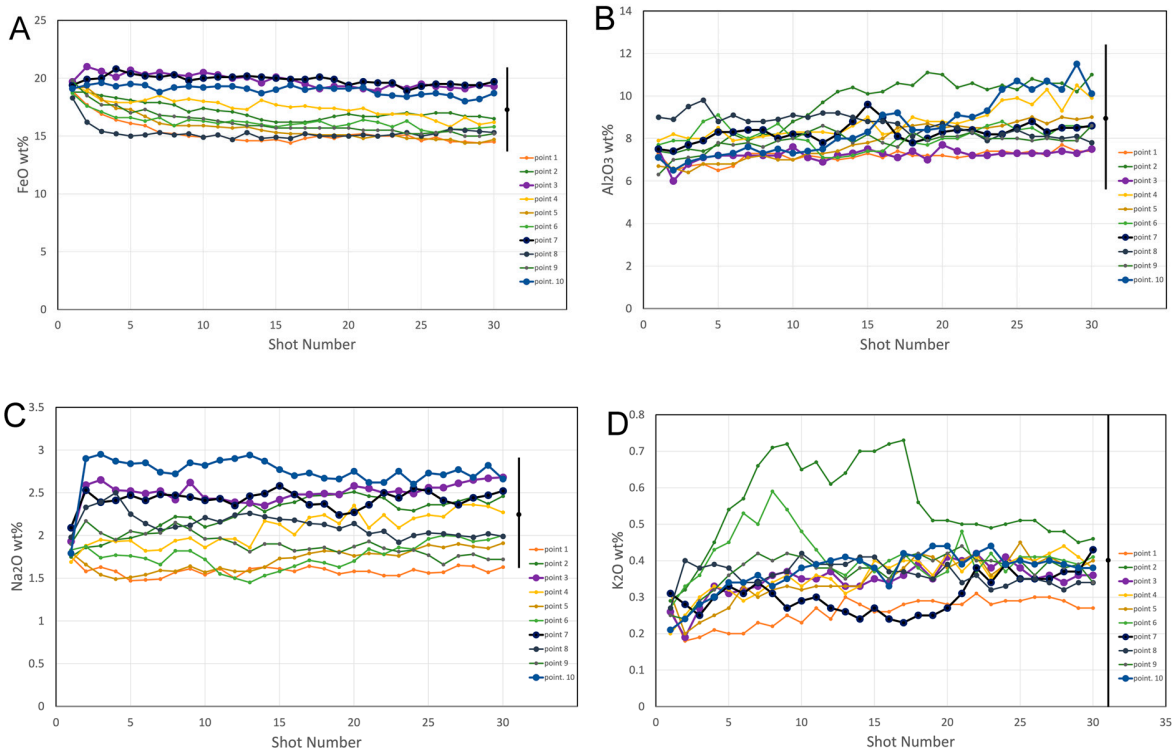

Figure S5. Additional ChemCam LIBS depth profiles of Groken nodules and surrounding materials on the Ayton_APXS_ccam raster scan (sol 2872). Target points are within areas of the APXS Ayton raster used to deconvolve the nodule composition (Table 3 of main text). Shot number refers to the sequential number of laser pulses at a given point, which is an unquantified proxy for depth into the target. Four of the targets (3, 7, 8, 10; darker colors, larger symbols) are on dark nodules (as shown in ChemCam RMI images); they show significant enrichments in MnO and also detections of P. Black bars show representative RMSEP uncertainties, including precision and accuracy relative to external standards. D) K_2O. RMSEP uncertainty is ~±0.6% wt (most of which would appear to be from calibration and not precision).

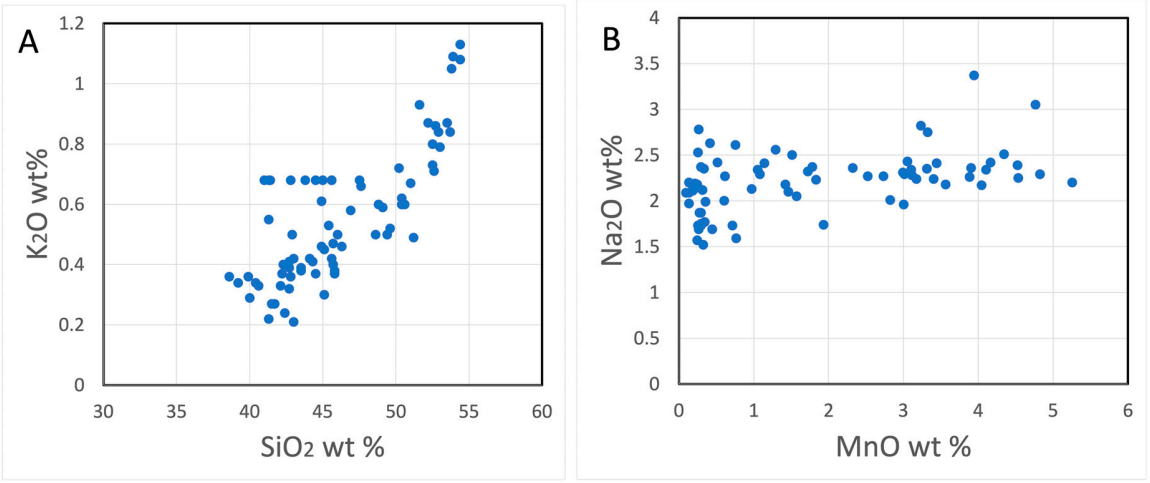

Figure S6. More ChemCam LIBS oxide abundances for spot target analyses in the Groken area. A) K_2O vs SiO_2. Following Dehouck, *et al.* [3], the high K (low Mg) and low-K (high Mg) components here are as observed across Glen Torridon. B) Na_2O vs MnO. Na abundances are effectively constant across all analyses.

LOCATIONS OF APXS AYTON AND LIBS CCAM ANALYSIS AREAS

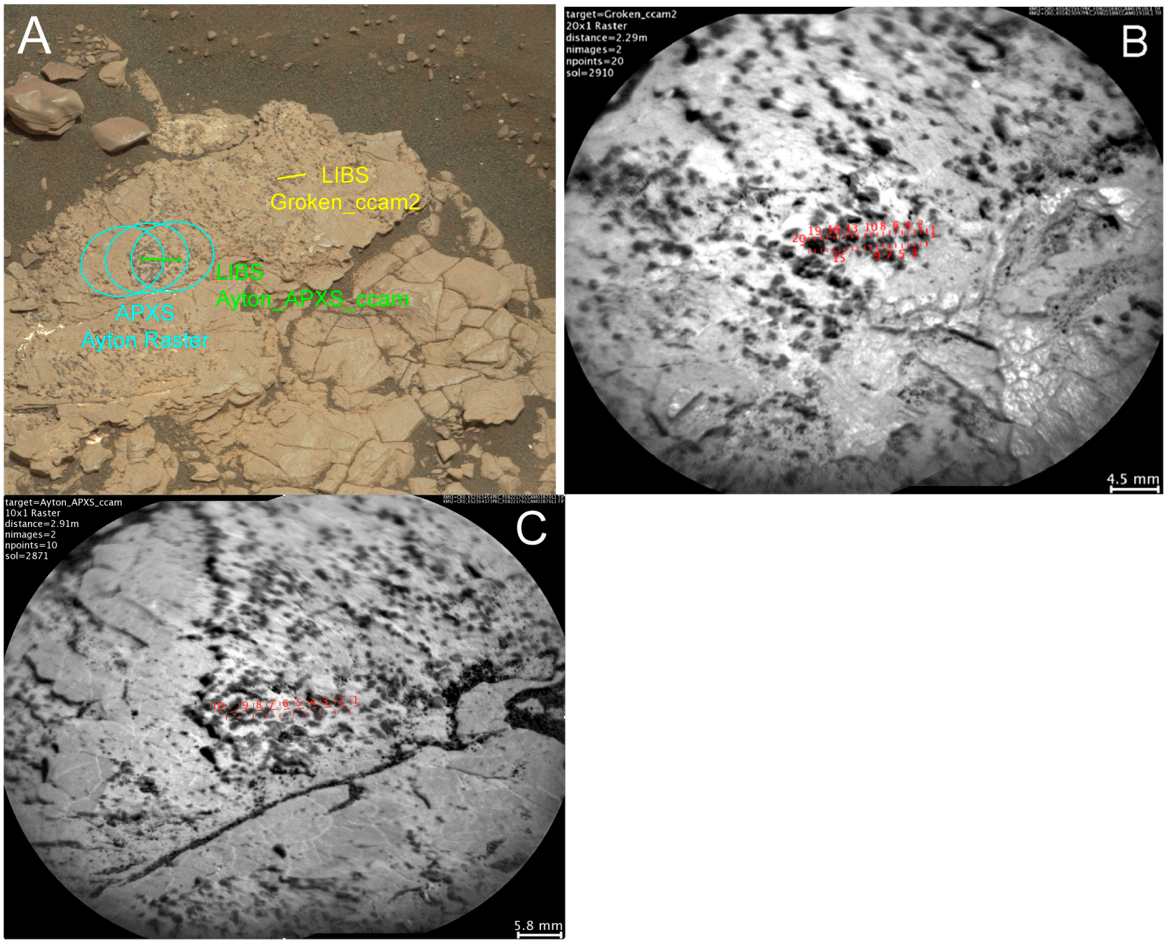

Figure S7. Locations of selected APXS and LIBS analyses referred to in text. A) Analysis area locations on Mozie_Law Slab (see Figures 3B and 4 of main text). Cyan ellipses are approximates location of the APXS Ayton raster; see Figure 9 of [2]. Yellow line is location of LIBS raster Groken_ccam2 (Table 4 of main text); green line is location of the LIBS raster Ayton_APXS_ccam (Figure 8 of main text). B) ChemCam RMI image mosaic of the area of LIBS raster Groken_ccam2. Twenty observation targets denoted in red. C) ChemCam RMI image mosaic of the area of LIBS raster Ayton_APXS_ccam. Ten observation targets denoted in red.

X-RAY DIFFRACTION: AMORPHOUS PHOSPHATES

Amorphous phosphate substances show broad X-ray diffraction bands centered around 30° 2θ for CuKα radiation [5-8]. Converting that angle for CheMin's CoKα radiation, amorphous phosphates should produce a broad hump centered around 36° 2θ (Figure S8). Diffraction patterns for other amorphous materials from [9][10][11].

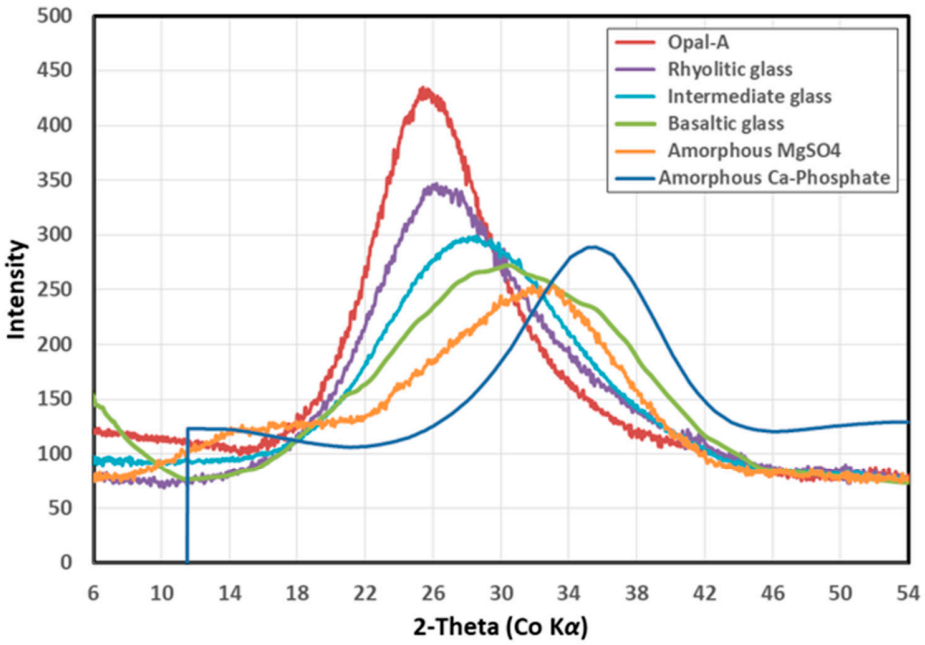

Figure S8. Expected diffraction pattern from amorphous phosphate substances (blue) compared to measured diffractions from amorphous silicate and sulfate materials.

MINERAL STABILITY CALCULATIONS

Equilibrium mineral stabilities were calculated and graphed using the code Geochemist's Workbench, GWB [12], augmented with manual calculations via spreadsheets. The thermochemical database used for calculations was that of Vieillard and Tardy [13] for consistency with the recent work of [14]. In the absence of many direct measurements, thermochemical data

on Mn-bearing phosphate minerals have been estimated or calculated using the assumptions of 'corresponding states' – that the properties of a phosphate phase can be estimated well as sums of properties of its constituent ions (e.g., Mn^{2+}), ionic groups (e.g., PO_4^{3-}), and molecules (e.g., H_2O). Nriagu and Dell [15] was perhaps the earliest attempt to estimate thermochemical properties for Mn-bearing phosphates. Vieillard and Tardy [13] produced a comprehensive self-consistent tabulation of thermochemical data for phosphates, solids and aqueous ions, but with very few Mn-bearing phases. La Iglesia [16] applied a similar method but again without Mn-bearing phases. The method was extended by [17] and [18], who developed a series of correlations between composition and free energy for apatite-structure phosphates (the ThermAp method), grounded in the [13] database. Drouet, Loche, Fabre and Meslin [14] extended their earlier results to include Mn-phosphates of other structure types, again grounded in the [13] database. Their values are included in the GWB thermochemical data file: ThermoddemV1.10_15dec2020.tdat. For the most part, these data are consistent with those of earlier compilations, including that used by [19].

For many of the phases considered here, like laueite and reddingite, measured thermochemical data are not available. We estimated those values using the method of Drouet, Loche, Fabre and Meslin [14], which allows direct comparison with that work and with [13]. Those values are given in Table S1, and the detailed calculations are in the supplemental spreadsheet file.

Mineral	DG_f^0 (kJ/mol)	DH_f^0 (kJ/mol)	S_f^0 (J/mol-K)	Log Ksp (25°C)	Log Ksp* (25°C)
Laueite $Mn^{2+}Fe^{3+}_2(PO_4)_2(OH)_2 \bullet 8H_2O$	-4921	-5684.1	630.1	-8.96	-
Reddingite $Mn^{2+}_3(PO_4)_2 \bullet 3H_2O$	-3683.7	-4067.1	412.3	-4.79	
Mn-Vivianite $Mn^{2+}_3(PO_4)_2 \bullet 8H_2O$	-4869.2	-5544.1	600.3	-4.72	-
Rockbridgeite $Fe^{2+}Fe^{3+}_4(PO_4)_3(OH)_5$	-4735.5	-5251.7	597.2	-10.71	
Solubility product for dissolution based on the $H_2PO_4^-$ ion.					
* Ksp values inferred here based on presence or abundance in terrestrial low-T environments.					

These newly estimated data were appended to ThermoddemV1.10_15dec2020.tdat data file, which is given here as a supplemental file ThermoddemV1.10_Groken_apr2023.tdat.

Phase diagrams were constructed with the Geochemist's Workbench suite of applications [12], especially the Act2 and Phase2 programs. We graphed predominance (Act2) and mineral presence (Phase2) in $f(O_2)$-pH space, comparable to a standard Pourbaix diagram, for ranges of aqueous activities for Mn^{2+}, Fe^{2+}, and $H_2PO_4^-$. Figure S8 here shows the predominance diagrams, with the dominant Fe-bearing ionic species; Figure 13 of the main text shows mineral presence diagrams.

Further, we use the abundances of minerals and other phases in nature (on Earth) as constraints on our calculations. Some phases and minerals are calculated to be present or common across T-$f(O_2)$-pH-composition space, but are not found or only found rarely; these include $MnHPO_4 \bullet 3H_2O$; rockbridgeite ($Fe^{2+}Fe^{3+}_4(PO_4)_3(OH)_5$), reddingite ($Mn^{2+}_3(PO_4)_2 \bullet 3H_2O$), and anhydrous $Mn^{2+}_3(PO_4)_2$. These phases are not included in the calculations (Table S1).

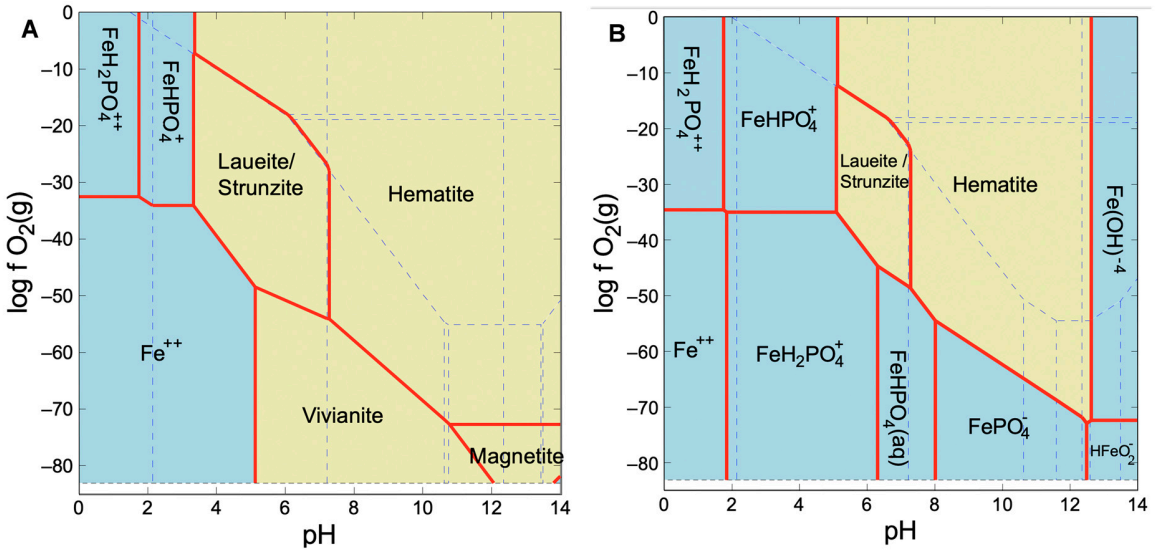

Figure S9. Species predominance diagrams for Fe-bearing solids and aqueous species relevant to stability of laueite/strunzite in solutions with Fe, Mn, and PO_4. Mn oxides and phosphates without Fe not shown. Calculated with the GWB Act2 program, see text and Supplemental Material. All diagrams for 25°C, 1 bar pressure, and dilute solution. Fields of aqueous species in blue and solids in yellow. Dashed lines are boundaries between other aqueous species (not shown). A) Log activities of: $H_2PO_4^-$, -2.9; Fe^{2+}, -6; Mn^{2+}, -3. B) Log activities of: $H_2PO_4^-$, -2.4; Fe^{2+}, -9; Mn^{2+}, -4.

VIVIANITE MORPHOLOGY

Figure 5D of the main text shows selected outlines of Groken nodules, and the text compares these outlines to the morphology of vivianite crystals. Here, we replicate that figure, and show line drawings and images of vivianite crystals.

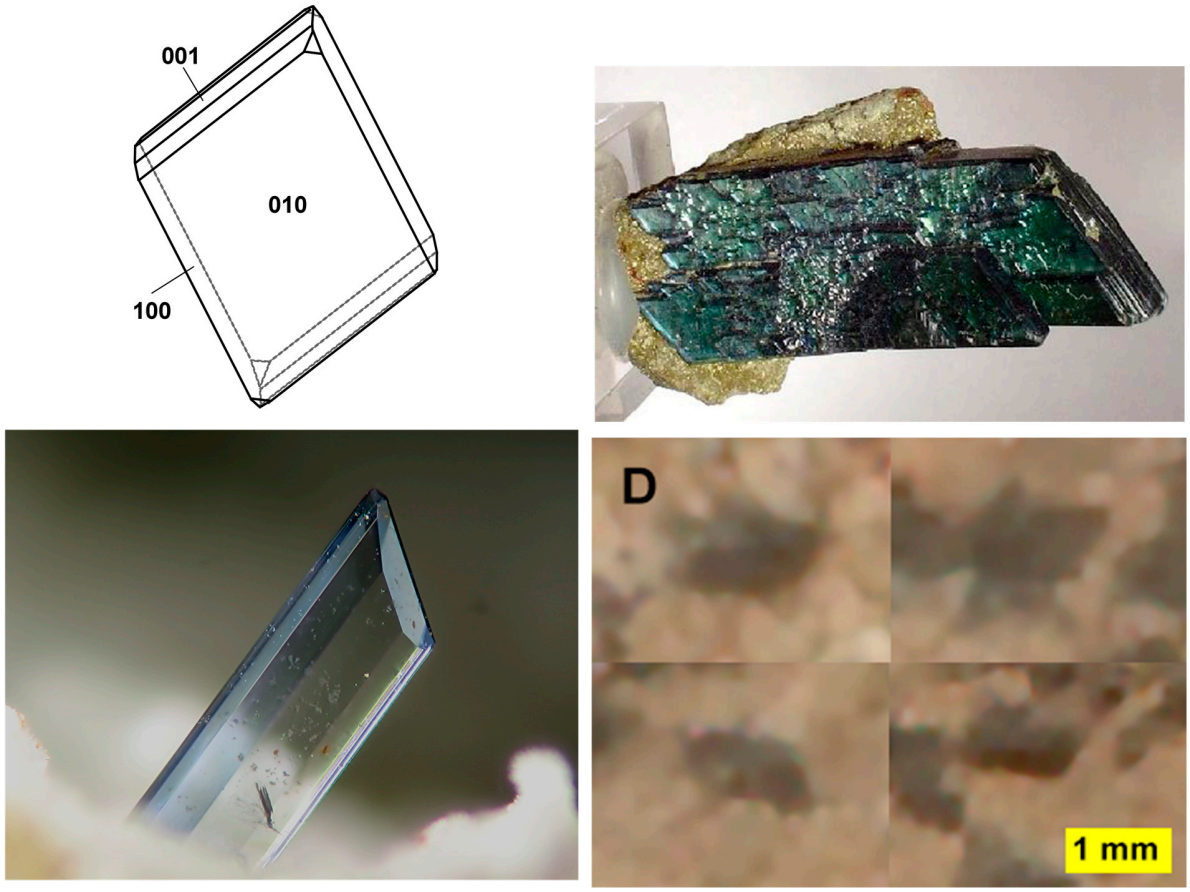

Figure S10. Morphology of vivianite single crystals, and selected Groken nodules. Details of Groken nodule textures, showing nodules' straight boundaries and sharp corners. A) Diagram of ideal single crystal of vivianite, showing edges and Miller indices of main faces [1]. B) Vivianite and childrenite, Siglo Veinte Mine, Bolivia. Copyright Rob Lavinsky, published under Creative Commons Attribution Share-Alike 3.0 (https://commons.wikimedia.org/wiki/File:Vivianite-Childrenite-117967.jpg). C) Vivianite crystal from the Hagendorf Süd pegmatite, FRG. Copyright Christian Rewitzer, published under Creative Commons Attribution Share-Alike 3.0 (https://commons.wikimedia.org/wiki:File:Vivianite-141168.jpg). D) Figure 5D of main text; nodules chosen to emphasize their angular outlines, and consistent minimum inter-edge angle of ~55°.

REFERENCES

1. Rečnik, A. *Minerals of the Mercury Ore Deposit Idria*; Springer 2013; p. 110.
2. VanBommel, S.J.; Berger, J.A.; Gellert, R.; O'Connell-Cooper, C.D.; McCraig, M.A.; Thompson, L.M.; Fedo, C.M.; Des Marais, D.J.; Fey, D.M.; Yen, A.S.; et al. Elemental composition of manganese- and phosphorus-rich nodules in the Knockfarril Hill member, Gale Crater, Mars. *Icarus* **2023**, *392*, 115372.
3. Dehouck, E.; Cousin, A.; Mangold, N.; Frydenvang, J.; Gasnault, O.; Forni, O.; Rapin, W.; Gasda, P.J.; Caravaca, G.; David, G. Bedrock geochemistry and alteration history of the clay-bearing Glen Torridon region of Gale crater, Mars. *Journal of Geophysical Research: Planets* **2022**, e2021JE007103.
4. Rice, M.S.; Seeger, C.; Bell, J.; Calef, F.; St. Clair, M.; Eng, A.; Fraeman, A.A.; Hughes, C.; Horgan, B.; Jacob, S. Spectral diversity of rocks and soils in Mastcam observations along the Curiosity rover's traverse in Gale Crater, Mars. *Journal of Geophysical Research: Planets* **2022**, *127*, e2021JE007134.
5. Ahmina, W.; El Moudane, M.; Zriouil, M.; Cherraj, M.; Taibi, M. Study of the mechanical and chemical properties of potassium manganese phosphate glasses. In Proceedings of the MATEC Web of Conferences, 2018; p. 01081.
6. Brangule, A.; Gross, K.; Komarovska, L.; Vīksna, A. Exploring zinc apatites through different synthesis routes. In Proceedings of the Key Engineering Materials, 2014; pp. 171-176.
7. Brangule, A.; Gross, K. Effect on drying conditions on amorphous calcium phosphate. In Proceedings of the Key Engineering Materials, 2015; pp. 99-103.
8. Vecbiskena, L.; Gross, K.A.; Riekstina, U.; Yang, T.C.-K. Crystallized nano-sized alpha-tricalcium phosphate from amorphous calcium phosphate: microstructure, cementation and cell response. *Biomedical Materials* **2015**, *10*, 025009.
9. Chipera, S.J.; Vaniman, D.T. Experimental stability of magnesium sulfate hydrates that may be present on Mars. *Geochimica et Cosmochimica Acta* **2007**, *71*, 241-250.
10. Lee, S.; Xu, H.; Xu, H. Reexamination of the structure of opal-A: A combined study of synchrotron X-ray diffraction and pair distribution function analysis. *American Mineralogist* **2022**, *107*, 1353-1360.
11. Chipera, S.J.; Vaniman, D.T.; Rampe, E.B.; Bristow, T.; Martinez, G.; Tu, V.; Peretyazhko, T.; Yen, A.S.; Gellert, R.; A., B.J.; et al. Crystallographic Investigation of Mg-sulfate at Gale Crater, Mars. *Science* **submitted**, *tbd*, tbd.
12. Bethke, C.M. *Geochemical and Biogeochemical Reaction Modeling*; Cambridge University Press: 2022; p. 543.
13. Vieillard, P.; Tardy, Y. Thermochemical properties of phosphates. In *Phosphate Minerals*; Springer: 1984; pp. 171-198.
14. Drouet, C.; Loche, M.; Fabre, S.; Meslin, P.-Y. On the occurrence of jahnsite/whiteite phases on Mars: A thermodynamic study. *American Mineralogist* **2022**, *107*, 1807-1817.
15. Nriagu, J.O.; Dell, C. Diagenetic formation of iron phosphates in recent lake sediments. *American Mineralogist* **1974**, *59*, 934-946.
16. La Iglesia, A. Estimating the thermodynamic properties of phosphate minerals at high and low temperature from the sum of constituent units. *Estudios Geológicos* **2009**, *65*, 109-119.

17. Drouet, C. A comprehensive guide to experimental and predicted thermodynamic properties of phosphate apatite minerals in view of applicative purposes. *Journal of Chemical Thermodynamics* **2015**, *81*, 143-159.
18. Drouet, C. Applied predictive thermodynamics (ThermAP). Part 2. Apatites containing Ni^{2+}, Co^{2+}, Mn^{2+}, or Fe^{2+} ions. *Journal of Chemical Thermodynamics* **2019**, *136*, 182-189.
19. VanBommel, S.J.; Gellert, R.; Berger, J.; McCraig, M.; O'Connell-Cooper, C.; Thompson, L.; Yen, A.; Boyd, N.; Lanza, N.; Ollila, A. Constraining the chemical depth profile of a manganese-rich surface layer in Gale crater, Mars. *Spectrochimica Acta Part B: Atomic Spectroscopy* **2022**, *191*, 106410.